J. Fluid Mech. (2019), *vol.* 861, *pp.* 860–885.
doi:10.1017/jfm.2018.939

The onset of dynamic stall at a high, transitional Reynolds number

S. I. Benton[1,†] **and M. R. Visbal**[1]

[1]Air Force Research Laboratory, Wright-Patterson AFB, OH 45433, USA

(Received 30 January 2018; revised 12 September 2018; accepted 19 November 2018; first published online 28 December 2018)

Dynamic stall due to a ramp-type pitching motion is investigated on the NACA 0012 airfoil at chord Reynolds number of $Re_c = 1.0 \times 10^6$ through the use of wall-resolved large-eddy simulation. Emphasis is placed on the unsteady boundary-layer interactions that develop as the airfoil approaches stall. At this Reynolds number it is shown that turbulent separation moves upstream across much of the airfoil suction surface. When turbulent separation reaches the leading-edge separation bubble, a bursting event is initiated leading to a strong coherent leading-edge vortex structure. This vortex wraps up the turbulent shear layer to form a large dynamic stall vortex. The use of large-eddy simulation elucidates the roll of the laminar separation bubble in defining the onset of the dynamic stall process. Comparisons are made to identical simulations at lower Reynolds numbers of $Re_c = 0.2 \times 10^6$ and 0.5×10^6. This comparison demonstrates trends in the boundary-layer mechanics that explain the sensitivity of the dynamic stall process to Reynolds number.

Key words: aerodynamics, boundary layers, vortex flows

1. Introduction

Dynamic stall refers to the unsteady separation of an airfoil boundary layer in a scenario where the time scales of the airfoil motion are of similar order to, or faster than, the times scales of the flow (inviscid and viscous). These events encompass a rich set of interactions that depend on a large parameter set including flow (Reynolds and Mach numbers), motion (pitch rate) and geometric (airfoil thickness and camber) parameters, to highlight the most prominent. This complex dependency makes successful prediction difficult. Large load fluctuations associated with abrupt flow changes and the development of large vortex structures make this a problem of continuing interest to vehicle designers. Comprehensive reviews of experimental test campaigns and computational approaches can be found in McCroskey (1982), Carr (1988) and Ekaterinaris & Platzer (1997).

The dynamic stall literature is vast and extends over more than a half-century. Due to the nature of the current work this brief review is mostly limited to works that have studied dynamic stall in a low-Mach number ($M_\infty \leqslant 0.2$) environment such that compressibility effects can be safely ignored. Ham (1967) is considered the first

†Email address for correspondence: stuart.benton.1@us.af.mil

study to describe the phenomenon of dynamic stall as a fundamental and generic fluid dynamic process encompassing a number of engineering concerns such as the stall-flutter instability and wing/gust interactions. The work isolates the delay of stall for an airfoil rapidly pitching above the static stall angle. This leads to the classic description of a continued increase in lift as the airfoil pitches above the static stall angle, culminating in the shedding of a low-pressure disturbance emanating from near the airfoil leading edge. This disturbance is the result of a shed vortex structure, which causes a transient lift increase and, as the vortex convects across the airfoil chord, a strong nose-down pitching moment. Later work by Ham (1972) first linked the development of this leading-edge dynamic stall vortex (DSV) structure with the presence of a laminar separation bubble (LSB) within the leading-edge suction surface boundary layer, prior to stall. These results, on the NACA 0012 airfoil at chord Reynolds number (Re_c) of 0.3×10^6, suggested that a bursting processes within the LSB was the mechanism for leading-edge vortex development. Similar observations have been made by additional experiments within a similar range of Re_c (Chandrasekhara, Carr & Wilder 1994; Schreck, Faller & Robinson 2002; Lee & Gerontakos 2004). Martin *et al.* (1974) also showed the presence of the LSB on the airfoil suction surface prior to stall, but could not experimentally resolve the bursting process. Their study included a range of Re_c spanning $0.3–3.0 \times 10^6$ and showed a strong sensitivity of the dynamic stall behaviour to Re_c, indicating that this range encompassed different types of stall processes. These results prompted a more extensive experimental campaign at the NASA Ames Research Center to perform parameter studies at more realistic Re_c as presented in Carr, McAlister & McCroskey (1977) and McAlister, Carr & McCroskey (1978) and later on at higher Mach number and for various airfoil sections (McAlister *et al.* 1982; McCroskey *et al.* 1982; Carr *et al.* 1982). Carr *et al.* (1977) focuses on the NACA 0012 airfoil at $Re_c \geqslant 10^6$ and coins the phrase 'abrupt leading-edge separation' to describe the dynamic stall process at these higher Re_c. In this process, a leading-edge vortex is formed as the turbulent-separation point rapidly propagates upstream to the airfoil leading edge causing leading-edge suction collapse. This description is opposed to the mechanism of LSB bursting, which had been the primary understanding of leading-edge separation, especially in the case of static stall.

These interactions are of relevance to the attempt to link dynamic stall characteristics to previous classifications of static stall processes, most prominently leading-edge and trailing-edge stall types (Jones 1934; McCullough & Gault 1951). In leading-edge stall, the LSB contracts with increasing angle of attack (α) to a point at which it is no longer able to facilitate turbulent reattachment due to the increasing pressure gradient. This results in a sudden separation of the airfoil boundary layer due to the bursting of the LSB. Leading-edge stall is associated with abrupt lift and moment stalls as well as a hysteresis between pitching directions. Trailing-edge stall, by contrast, occurs in a situation of no LSB or a stable LSB and describes the relatively slow upstream propagation of turbulent boundary-layer separation from the airfoil trailing edge up to the leading edge, resulting in gradual lift and moment stall with little hysteresis. The dynamic counterpart of trailing-edge separation would not necessarily be expected to generate a leading-edge vortex structure. This results in the use of the term abrupt leading-edge separation to contrast the development of a leading-edge vortex from a trailing-edge stall type process instead of a leading-edge stall behaviour. A discussion is included in McCroskey, Carr & McAlister (1976) on the role of the LSB in abrupt leading-edge separation where the use of a boundary-layer trip, a reduced leading-edge radius and a cambered leading-edge are each used to contrast

the stall behaviour under direct manipulation of the state of the leading-edge LSB. It was concluded that the LSB played little role in the dynamic stall process. However, the process relies on the rapid movement of the turbulent separation upstream from approximately 10 % chord to the leading edge. This process would be facilitated by the turbulent separation interacting with a laminar separation bubble. McCroskey *et al.* (1976) alludes to this and references earlier works by Evans & Mort (1959) and Wallis (1962) which describe interactions between turbulent separation and a leading-edge LSB that could be characterised as a 'second' type of leading-edge stall. However, at this scale, these boundary-layer mechanics could not be fully visualised or measured experimentally and the discussion relies on semi-empirical computations and inferences from parametric studies. Furthermore, later works (Chandrasekhara, Wilder & Carr 1996) discussed the particular difficulty in effectively tripping the suction-surface boundary layer in a dynamic stall situation which calls into question whether or not the LSB was entirely removed in the parametric study of McCroskey *et al.* (1976).

Leishman (1984, 1990) highlighted similar inconsistencies when comparing the dynamic stall behaviour of the NACA 23012 airfoil at $Re_c = 1.5 \times 10^6$ to its static stall counterpart. He reported a leading-edge type stall behaviour in the dynamic scenario when the airfoil was otherwise classified to exhibit trailing-edge stall in static conditions. Leishman (1990) presented instantaneous wall pressure histories that show a strong, rapid 'sharp transient' in suction just prior to the development of the dynamic stall vortex. In this article, Leishman describes this sharp transient as an upstream effect of a DSV that develops at approximately 10 % chord downstream of the leading edge, however no flow field measurements are available to support this statement. Further data in Leishman (1984) showed this feature to be consistent over variations in pitching parameters given a high maximum angle and a high pitch rate. Recent experimental results (Gupta & Ansell 2018) have recovered the same low-pressure transient. This feature appears to be unique to the abrupt leading-edge separation process and is so far unexplained. Prior to leading-edge suction collapse, studies such as Lorber & Carta (1988) at $Re_c = 2.0 \times 10^6$ have noted increased unsteadiness in pressure near the leading edge. Recent computations at $Re_c = 0.2 \times 10^6$ and 0.5×10^6 by Visbal & Garmann (2018) and Visbal (2014*a*) recovered the same unsteadiness linking it to acoustic radiation emanating from the leading-edge LSB. This unsteadiness was also noted by Gupta & Ansell (2018) experimentally at both $Re_c = 0.5 \times 10^6$ and 1.0×10^6.

Modern experiments that rely heavily on the use of particle image velocimetry, such as those by Mulleners & Raffel (2012, 2013) and Pruski & Bowersox (2013), have focused on the formation process of the DSV. Using these techniques, the DSV is shown to develop through the amalgamation of turbulent structures and can be, for a brief period of time, fed by the leading-edge separated shear layer before convecting downstream. Pruski & Bowersox (2013) specifically observed Kelvin–Helmholtz-type structures in the separated shear layer feeding into the DSV. Mulleners & Raffel (2013) described the breakdown of the separated turbulent shear layer above the thin region of reverse flow and the process by which these structures merge in the development of the DSV.

The lack of understanding of these complex interactions highlights the need for a research technique that is capable of resolving the rapid events which occur within the transitional boundary layer. Wall-resolved large-eddy simulation (LES) is particularly well suited to provide better information about these details. Recent advances in efficient numerical techniques as well as a greater availability of computational

resources have made it possible to approach the type of problems described above with LES. Visbal (2014*b*, 2015) and Visbal & Garmann (2018) recently introduced the use of wall-resolved LES in the study of the events that lead to the onset of dynamic stall for a NACA 0012 airfoil operating at $Re_c = 0.2\text{–}0.5 \times 10^6$. For these conditions, a leading-edge LSB was shown to contract to a length approaching 3 %–7 % chord before bursting to form the DSV. At $Re_c = 0.5 \times 10^6$ a region of separated flow near the trailing edge developed and began to propagate upstream. However, it was shown that LSB bursting occurred before the separation point reached the LSB. These studies also noted hysteresis in the upstream movement of the suction-surface transition point while pitching up from a low angle of attack. These non-equilibrium turbulent features, the aforementioned high-frequency acoustic radiation, as well as the small spatial scales of the LSB highlights the needs for high-fidelity computations capable of resolving each of these features.

Given that there is experimental evidence of the presence of suction surface LSBs up to Reynolds numbers of the order of 10^7 (Tani 1964), the present study seeks to extend the use of wall-resolved LES to higher Re_c. Trends at lower Re_c suggest that an increase in Reynolds number delays pressure-gradient-induced bursting of the LSB to higher α, thus allowing for separation development within the turbulent boundary layer. The present work (preliminary data were presented in Benton & Visbal 2017) extends the work of Visbal & Garmann (2018) to the much higher Re_c of 1.0×10^6. For the first time, the unsteady boundary-layer interactions that initiate the eventual formation of the DSV, at this condition, are described. It is settled that a direct interaction between a small leading-edge LSB and the upstream-propagating turbulent separation results in a complex leading-edge stall process. The interplay between these boundary-layer features helps to elucidate the mechanisms responsible for the sensitivity of the dynamic stall process to Re_c within the range of $10^5\text{–}10^6$. Note that in this methodology, a three-dimensional finite-span domain with periodic boundary conditions is specified. In order to allow for a practical simulation, the span is extended to the point at which all important scales in the transitional and turbulent boundary layer are resolved, but is otherwise limited such that very long-wavelength behaviours, such as stall cells, are precluded. The simulation begins with a statistically stationary solution at $\alpha = 8^\circ$ and $Re_c = 1.0 \times 10^6$. Through a brief acceleration period the airfoil pitch rate is increased to the constant, non-dimensional value of $\Omega_0 = \Omega c/U_\infty = 0.05$. Section 2 discusses the numerical approach used in this work and § 3 describes the problem specification and the grid details. In the results (§ 4) the flow development is described in chronological order beginning with the initial condition (§ 4.1) and an overview of the dynamic stall process (§ 4.2). This leads into descriptions of the contraction of the LSB and the upstream propagation of the turbulent separation as the airfoil pitches (§§ 4.3 and 4.4). When these two features meet, a bursting process occurs (§ 4.5) which results in a system of vortex structures that merge to form the DSV (§ 4.6). Finally, concluding statements are made in § 5.

2. Numerical approach

The governing equations are the fully three-dimensional, compressible, unfiltered, Navier–Stokes equations cast in the strong conservative form utilising a general time-dependent curvilinear coordinate transformation from physical to computational space (Vinokur 1974; Steger 1978). Non-dimensionalisation is performed using the free-stream values and the airfoil chord (c), with the exception of static pressure which is non-dimensionalised by twice the free-stream dynamic pressure $\rho_\infty U_\infty^2$. Pressure, density and temperature are related through the ideal gas law.

All simulations are performed with the extensively validated high-order Navier–Stokes solver FDL3DI (Gaitonde & Visbal 1998; Visbal & Gaitonde 1999). In this code, a finite-difference approach is employed to discretise the governing equations, and all spatial derivatives are obtained with sixth-order compact-differencing schemes (Lele 1992). Time marching is accomplished through a second-order, iterative, implicit, approximately factored method (Beam & Warming 1978).

For the case of a pitching airfoil, the grid is moved in a rigid fashion using the prescribed airfoil motion. To ensure that the geometric conservation law is satisfied, the time metric terms are evaluated employing the procedures described in Visbal & Gaitonde (2002).

In order to eliminate spurious components, a high-order lowpass spatial filtering technique (Gaitonde, Shang & Young 1999; Visbal & Gaitonde 1999) is introduced. A compact formulation based on templates proposed by Lele (1992) and by Alpert (1981) and with proper choice of coefficients, provides a $2N$th-order formula on a $2N + 1$ point stencil. These coefficients, along with representative filter transfer functions, can be found in Gaitonde & Visbal (1998). The filter is applied to the conserved variables along each transformed coordinate direction once after each time step or sub-iteration.

The above numerical methods are applied to the original unfiltered Navier–Stokes equations, and are used without change in laminar, transitional, or fully turbulent regions of the flow. For turbulent regions of the flow field these high-fidelity spatial algorithmic components provide an effective implicit LES approach in lieu of traditional sub-grid stress models, as demonstrated in Visbal & Rizzetta (2002), Rizzetta, Visbal & Blaisdell (2003) and Garmann, Visbal & Orkwis (2013). In regions of laminar and early-stage transition this methodology is effectively a direct numerical simulation of the Navier–Stokes equations, therefore this approach is well suited for the study of unsteady flows highly coupled to transitional processes.

3. Problem specification

3.1. *Preliminary considerations*

Computations are performed for the NACA 0012 wing section. This symmetric section with 12 % maximum thickness and leading-edge radius $r/c = 0.0158$ has been used in numerous experimental and computational dynamic stall investigations. In order to avoid major compressibility effects, a low free-stream Mach number $M_\infty = 0.1$ is specified.

The grid is shown in figure 1. The original sharp trailing edge is rounded with a very small circular arc ($r/c = 0.0018$) in order to facilitate the use of an O-mesh topology. Sectional two-dimensional grids are used to construct the three-dimensional mesh in the spanwise direction, with uniform Δz spacing, to a spanwise extent of $S/c = 0.05$. This O-grid is then divided into a system of four nested O-grid blocks. The Chimera overset technique with high-order interpolation (Sherer & Visbal 2007) is applied to transfer information between blocks. This allows for successive coarsening in the azimuthal and spanwise directions in regions far from the airfoil, which would otherwise be restricted to resolution requirements dictated by the turbulent boundary layer. The grid used in the current study is comprised of 267×10^6 nodes. Further details on grid dimensions, spacing, and sensitivity are discussed in detail in appendix A, along with an extended discussion of the choice of spanwise domain size.

Along the airfoil surface, a no-slip adiabatic condition is employed in conjunction with a zero normal pressure gradient. The surface velocity components are determined

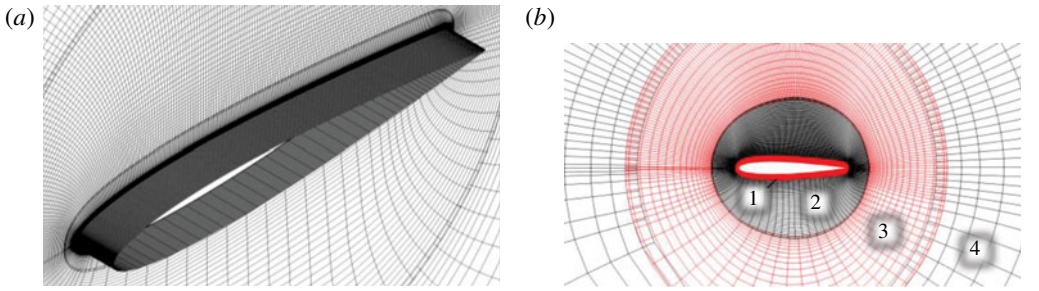

FIGURE 1. (Colour online) Isometric (*a*) and side (*b*) views of nested O-grid topology, every fourth point shown.

from the imposed pitching motion, and are otherwise set to zero for static cases. Along the far field boundary, located 100 chords away from the airfoil, free-stream conditions are specified. In the far field an absorbing sponge zone, as described by Zhou & Wang (2010), is introduced. This region is slowly implemented between $50c$ and $70c$ away from the airfoil at which point it is fully applied to the end of the domain. Spatially periodic conditions were enforced in both the azimuthal and spanwise (homogeneous) directions using five-plane overlaps.

Computations are performed with a time step of $\Delta t U_\infty/c = 1 \times 10^{-5}$. This results in nearly 35 000 time steps per degree of rotation. For pitching simulations the entire flow solution is output at a non-dimensional time of 0.02. Additionally, flow properties on the airfoil suction surface and the three nearest grid planes (in order to compute wall velocity gradients) are output corresponding to a non-dimensional time of 0.001.

3.2. *Pitching motion*

This study examines dynamic stall onset on an airfoil pitching at a constant rate. The solution is initiated with a statistically stationary solution at $\alpha = 8°$. To transition into the ramp-type motion, the angular velocity is slowly increased from zero to the constant value of $\Omega_0 = 0.05$. This is accomplished using the expression

$$\dot{\alpha}(t) = \Omega_0(1 - \mathrm{e}^{-4.6t/t_0}), \tag{3.1}$$

where Ω_0 is the eventual constant pitch rate and the angular velocity reaches 99 % of its final value within the initial time window specified by t_0 (Visbal & Shang 1989). Equation (3.1) is integrated to give the instantaneous angle of attack (3.2):

$$\alpha(t) = \Omega_0[t + t_0/4.6(\mathrm{e}^{-4.6t/t_0} - 1)] + \alpha_0. \tag{3.2}$$

For the ramp-type motion in this document, pitching begins at $\alpha_0 = 8°$, the constant pitch rate is set at $\Omega_0 = 0.05$ and the acceleration decays within the first $t_0 = 0.5$. Pitching is performed about the airfoil quarter-chord location. To facilitate conversion between reported α and time, it is noted that this pitch rate corresponds to 2.86° per convective time or 0.35 time units per degree.

4. Results

4.1. *Initial condition at $\alpha = 8°$*

To begin, a statistically stationary solution at $\alpha = 8°$ is computed. The grid is oriented such that the airfoil is horizontal (as shown in figure 1*b*) with the initial α being

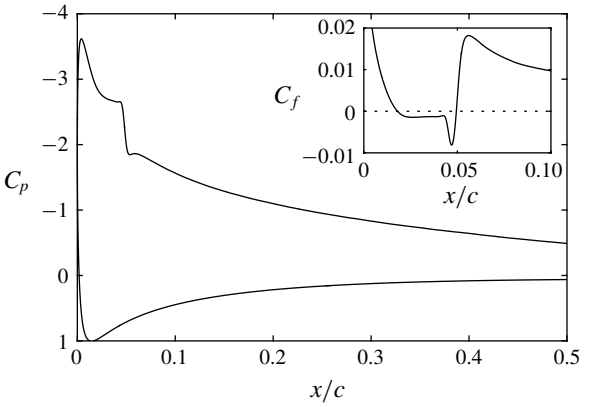

FIGURE 2. Time-mean wall pressure coefficient for the static solution at $\alpha = 8°$. The inset shows the wall skin-friction coefficient in the vicinity of the laminar separation bubble.

set in the free stream. At this condition, the airfoil boundary layer is characterised by a small LSB near the leading edge that is responsible for the transition of the upper surface boundary layer to turbulence. The signature of the bubble is shown in figure 2 in both the pressure and skin-friction coefficients. As can be inferred from the inset in figure 2, the boundary layer separates at $x/c = 0.018$ and reattaches at $x/c = 0.05$, giving a bubble length (in surface distance) of $L/c = 0.034$. The pressure surface boundary layer is laminar from the stagnation point to the trailing edge.

This condition of $\alpha = 8°$ is chosen to minimise computational requirements for the simulation of the onset of dynamic stall at computationally demanding Reynolds numbers of $O(10^6)$. The angle is high enough to ensure a laminar boundary layer on the pressure surface for the entirety of the computation, but low enough such that the constant pitch rate can be achieved well below the point at which the airfoil pitches above the static stall angle, $\alpha = 12°$–$14°$ (Critzos, Heyson & Boswinkle Jr 1955; Sheldahl & Klimas 1981).

4.2. *Overview of dynamic stall development*

A general overview of the dynamic stall process is first given before a more in-depth discussion of the specific boundary-layer and vortex interactions are presented. Beginning at $\alpha = 8°$, a short acceleration period is specified. This transitions the airfoil motion to the constant pitch rate of $\Omega_0 = 0.05$, which is then maintained to the point at which the simulation is terminated. All visualisations of the flow solution are presented with the grid pitched relative to the initial condition of $\alpha = 8°$.

The force history for the manoeuvre is shown in figure 3 with shaded regions highlighting the various stages of boundary-layer and vortex development that describe the onset of dynamic stall. Each of these stages is described in detail in the following sections. Many of the trends in the force history are classic in dynamic stall research namely the high normal force coefficient (C_n) above the static stall angle with a peak that corresponds to vortex development. Note that when the simulation is terminated ($\alpha \approx 30°$), the DSV has propagated to $x/c = 0.6$ and C_n would be expected to drop suddenly once the vortex has convected past the trailing edge. At approximately $\alpha = 20°$ there is a sudden rise in the drag coefficient (C_d) as well as a roll off in the quarter-chord moment coefficient ($C_{m,c/4}$), both of which are due to the effective

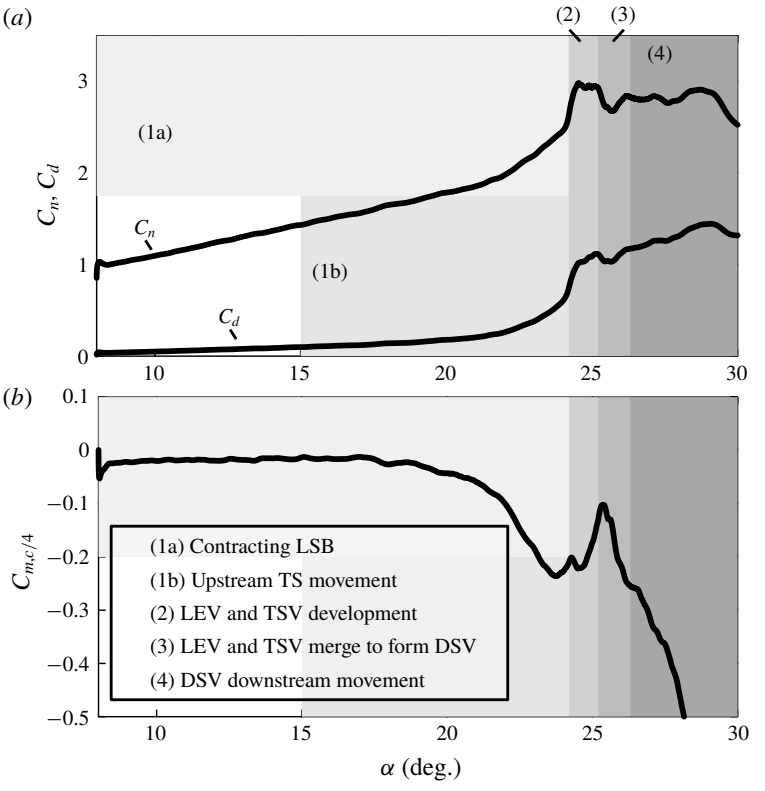

FIGURE 3. Force coefficients as a function of α showing the dynamic stall process.

thickening of the airfoil upper surface due to the reversed flow within the turbulent boundary layer. A brief reversal of the trend in moment coefficient is noted at the point of vortex development. This transitions to a rapid increase in the negative moment once the DSV begins to convect downstream.

For $Re_c = 1.0 \times 10^6$ the stages of the onset of dynamic stall listed and highlighted in figure 3 are visualised in figures 4(*c*) and 5. In figure 4, a spatio-temporal contour of skin-friction coefficient (C_f) illustrates the contraction of the small region of reverse wall shear associated with the leading-edge LSB, which occurs for each Re_c. At $\alpha \approx 15°$, turbulent separation (TS) appears near the trailing edge. This is marked with a dashed line and is shown to propagate upstream. Figure 4(*a*,*b*) show similar LSB contraction and upstream TS propagation at the lower Reynolds numbers of $Re_c = 0.2 \times 10^6$ and 0.5×10^6. At each lower Re_c shown here, dynamic stall develops from the bursting of the leading-edge LSB (Visbal 2014*b*; Visbal & Garmann 2018). It should be noted that these data at lower Re_c are from new computations beginning with $\alpha_0 = 8°$ to allow for direct comparison to $Re_c = 1 \times 10^6$. Comparison with the previous results (which began at $\alpha_0 = 4°$) from Visbal (2014*b*) and Visbal & Garmann (2018) are excellent. With increasing Re_c the LSB is more stable to the bursting process which allows for further upstream propagation of TS before the DSV develops.

The case of $Re_c = 1.0 \times 10^6$ represents a transition to a new form of dynamic stall within which the LSB exists but is stable to the bursting process and TS is able to propagate upstream to the LSB. The development of the vortex structures

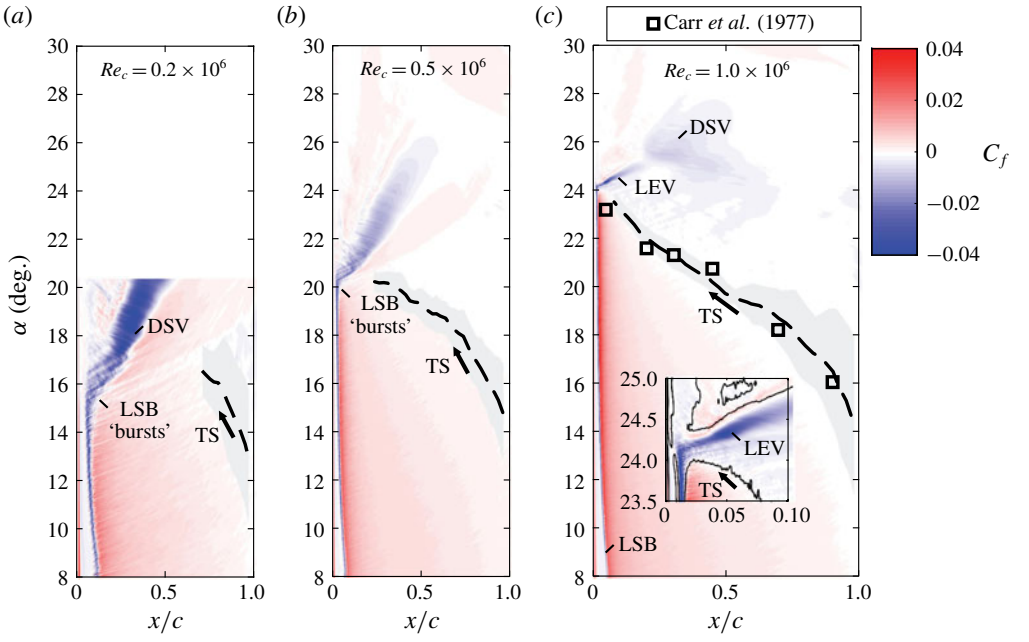

FIGURE 4. (Colour online) Spatio-temporal (x–α) contours of span-averaged wall skin-friction coefficient on the airfoil suction surface. Data at the lower Reynolds numbers of $Re_c = 0.2 \times 10^6$ (a) and 0.5×10^6 (b) are included for comparison.

from these boundary-layer interactions is illustrated using select instantaneous mid-span contours of entropy in figure 5 (a corresponding animation is made available in the supplementary material at https://doi.org/10.1017/jfm.2018.939). At $\alpha = 24°$ the TS point has propagated upstream and meets the turbulent reattachment point of the LSB (event 1 in figure 5). This causes a bursting event that results in the development of a small leading-edge vortex (LEV) structure. Meanwhile, the turbulent boundary layer is separated over nearly 98 % of the airfoil suction surface and has begun to roll up to form a second vortex structure termed the turbulent-separation vortex (TSV) in this work (event 2). These structures merge as the LEV wraps up the TSV, pulling it slightly upstream (event 3). This final vortex structure is referred to as the DSV, in the classical sense used in the literature. The DSV then propagates downstream as is typically observed. After formation of the DSV, the simulation is terminated as it is known that the interaction between the DSV and the trailing edge, is highly dependent on full wing geometry and longer-wavelength instabilities not captured in the current spanwise-periodic slice.

The following sections describe these events in further detail with an emphasis on the unsteady boundary-layer mechanics that result in the onset of dynamic stall. At Re_c of $O(10^6)$ the boundary layer becomes increasingly difficult to resolve experimentally due to its decreasing thickness and the unsteady motion of the airfoil surface. This indicates that high-fidelity computations, such as the current study, are particularly well suited to study these events.

4.3. *Laminar separation bubble development*

A primary conclusion of the current study is that, despite a relatively high airfoil Re_c and a very small LSB, the LSB is crucial in the overall development of the DSV and

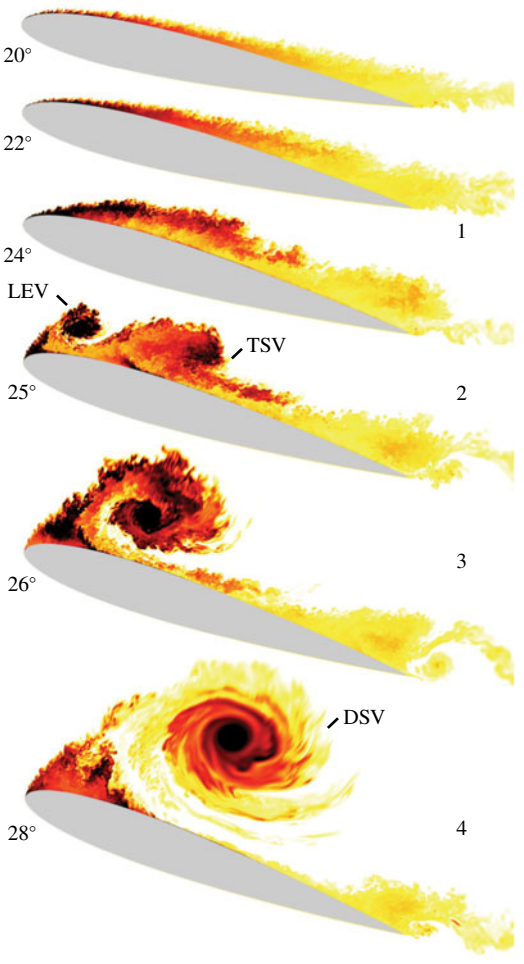

FIGURE 5. (Colour online) Instantaneous contours of entropy at the mid-span showing overall process of dynamic stall. Numbers refer to the list of events in figure 3. An animation of this contour is included in the supplementary material.

ultimately sets the inception point of the DSV. Accurately accounting for the effect of the LSB is key to locating the DSV and predicting the pressure loads during the unsteady stall process.

As described for the static condition at $\alpha = 8°$ the LSB is located near the leading edge with an initial length of $L/c = 0.034$. As the airfoil pitches up, the flow acceleration around the leading edge increases, resulting in a higher peak suction as well as a stronger adverse pressure gradient across the LSB. Plots of LSB length and suction-surface minimum pressure coefficient ($C_{p,min}$) are included in figure 6. For reference, similar data at lower Re_c are included. At each of the lower Re_c a sharp increase in the LSB length occurs associated with the onset of pressure-gradient-induced LSB bursting. This does not occur at $Re_c = 1.0 \times 10^6$, where the LSB breaks down due to interaction with the turbulent separation. With increasing Re_c there is a strong reduction in the LSB length, corresponding to the strong sensitivity of the dynamic stall process to Re_c within the range

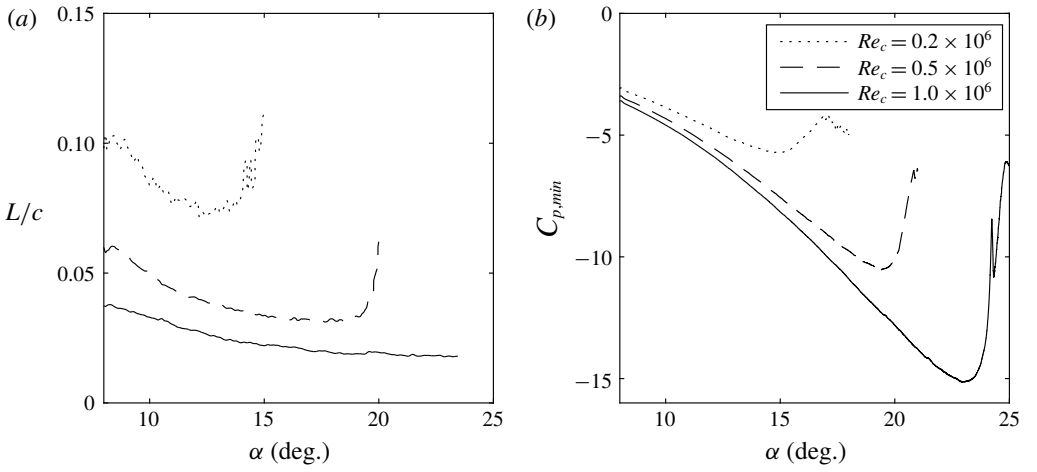

FIGURE 6. LSB length (*a*) and span-averaged minimum suction surface C_p (*b*) each as a function of α. Data at lower Re_c are included for comparison.

presented here. For $\alpha = 8°$ the length of the LSB as a function of Re_c is shown to be proportional to $Re_c^{-1/2}$ as might be expected. This suggests (preliminary computations at $Re_c = 1.5 \times 10^6$ confirm this) that the sensitivity of the dynamic stall process for $Re_c > 1.0 \times 10^6$ is likely reduced as suggested by Carr *et al.* (1977) and Leishman (1990).

Before vortex development, the leading-edge flow structure is characterised by a contraction of the LSB from $L/c = 0.034$ to 0.02. Simultaneously, peak suction increases from $C_p = -4$ to -15 suggesting flow acceleration up to four times U_∞ resulting in a local Mach number as high as $M_\infty = 0.5$, despite the low free-stream Mach number of 0.1. The fact that under this high adverse pressure gradient, no pressure-gradient-induced bursting is observed is an interesting conclusion. Preliminary attempts to apply bursting criteria from the literature (Tani 1964; Diwan, Chetan & Ramesh 2006) were made, but with little success. It is likely that a successful bursting criteria in the current situation must take into account the effects of the unsteady motion. This is an area requiring further study.

4.4. *Trailing-edge separation movement*

For $Re_c = 1.0 \times 10^6$, turbulent separation begins to appear at the trailing edge as the airfoil pitches past $\alpha \approx 15°$. Turbulent separation is marked by a black dashed line in figure 4 with a grey shaded region that represents two standard deviations of the recorded instances of zero wall shear. This relative unsteadiness of the separation location decreases as the TS point moves upstream with increasing α. After appearing at the trailing edge, the TS propagates upstream at a rate of $0.3U_\infty$ with a slight acceleration to $0.5U_\infty$ by the time separation reaches mid-chord. After this point, upstream propagation decelerates and continues at a mostly constant rate of $0.4U_\infty$ toward the leading edge. From approximately $x/c = 0.06$ to the reattachment point of the LSB the TS movement accelerates rapidly, as shown in the inset figure in figure 4(*c*) and discussed further in the next section. This is the precursor to LEV development.

As an implicit validation of the current simulation, as well as a demonstration of the applicability of the current ramp-type motion to understanding sinusoidal pitching,

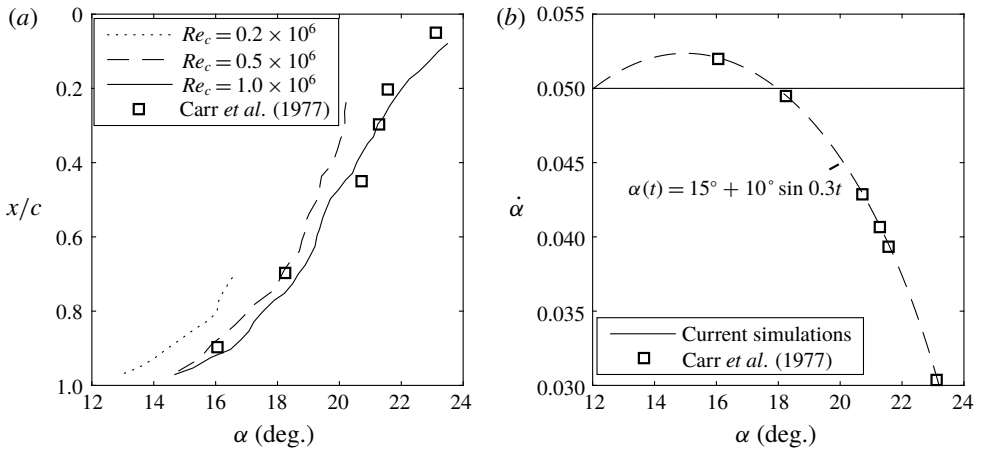

FIGURE 7. Turbulent-separation location (*a*) and pitch rate comparison against Carr *et al.* (1977) (*b*) each as a function of α. Data at lower Re_c are included for comparison.

the location of the TS is compared against data presented by Carr *et al.* (1977) at the same Re_c. This comparison is made as a function of α in both figures 4(*c*) and 7(*a*). A comparison of the pitch rate as a function of α is included in figure 7(*b*), where a thin dashed line shows the sinusoidal motion prescribed experimentally and black squares highlight the points in the motion where the location of the TS had been recorded. The comparison between the two motions is facilitated by the generally similar pitch rates (within the range $10^\circ \leqslant \alpha \leqslant 20^\circ$) and the observation made experimentally (Carr 1988) that favourable comparisons of dynamic stall behaviour are observed when the pitch rate at the static stall angle is consistent. Given the highly unsteady location of the TS and the somewhat large experimental uncertainty documented by Carr *et al.* (1977) this agreement is excellent. This comparison suggests that the turbulent boundary layer is properly resolved in order to predict the large momentum containing structures that determine averaged features such as turbulent separation.

4.5. *Bursting due to LSB/TS interaction*

At the point at which the TS reaches the turbulent reattachment point of the LSB a complex series of events are initiated. Regions of span-averaged reverse flow ($U_x < 0$, airfoil frame of reference) are highlighted in figure 8. As described by Carr *et al.* (1977) a thin region of reverse flow develops over the majority of the airfoil suction surface. Periodic undulations in the outer boundary indicate low-frequency large structures in the separated turbulent boundary layer, a feature that was also noted using smoke visualisations in Carr *et al.* (1977). The expanded views on the left of figure 8 show the upstream extent of the TS point and the small region associated with the recirculating flow within the LSB. At $\alpha = 24.08^\circ$ the two regions meet and by $\alpha = 24.36^\circ$ a distinct feature associated with the LEV is apparent. This interaction is expanded further in figure 9 to illustrate the development of the LEV directly from the LSB. The region of strong reverse flow, which terminates the chordwise extent of the LSB, develops continuously into the reverse flow associated with the LEV. This transition is shown through instantaneous snapshots of the skin-friction profile in the leading-edge region as well as contours of instantaneous vorticity in figures 9(*b*)

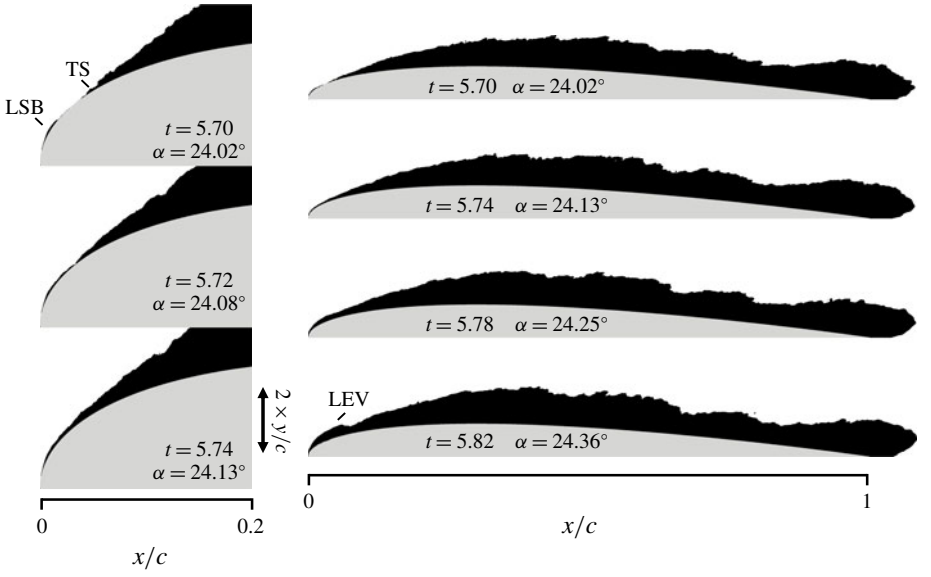

FIGURE 8. Regions of reverse flow ($U_x < 0$, black) in the airfoil frame of reference for select instances leading to LEV development. Note in the expanded figures on the left, the y-direction is scaled by a factor of two for clarity.

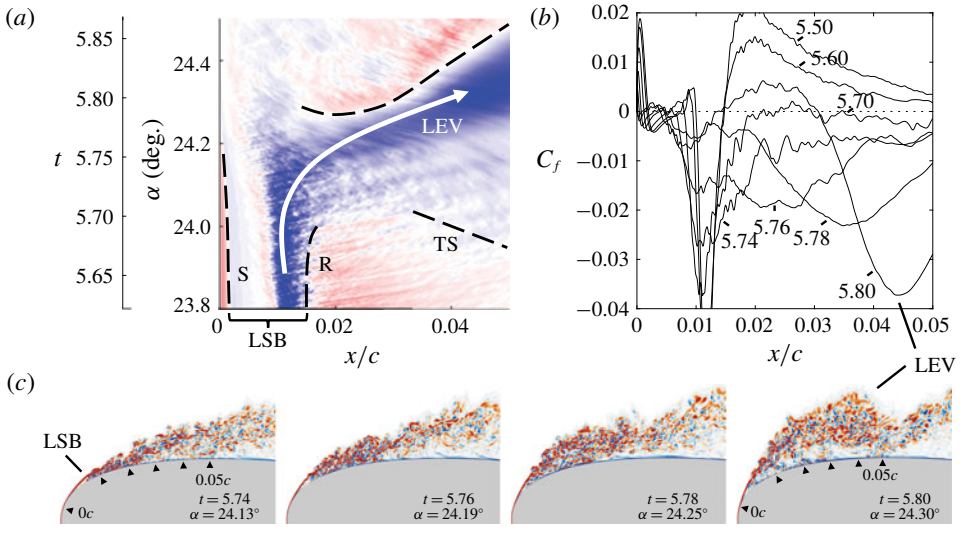

FIGURE 9. (Colour online) Spatio-temporal contour of span-averaged skin-friction coefficient (*a*) alongside instantaneous skin-friction profiles (*b*) and instantaneous contours of spanwise vorticity (*c*) each illustrating the development of the LEV from the leading-edge LSB. Carets mark x/c locations in increments of $0.01c$ in (*c*).

and 9(*c*), respectively. During the formation of the LEV (illustrated in figure 9*c*) vorticity is fed into this vortex structure directly from the leading-edge shear layer as well as the roll up of the near-stagnant turbulent boundary layer vorticity just downstream of the LSB.

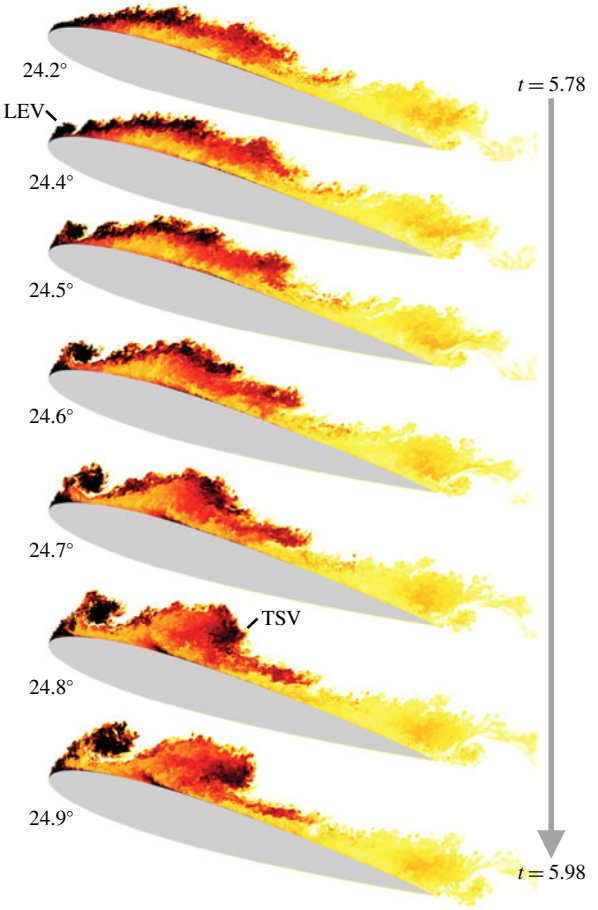

FIGURE 10. (Colour online) Contours of entropy showing rapid development of LEV.

A series of instantaneous mid-span contours of entropy are included in figure 10 to illustrate the development of the LEV and TSV structures. Corresponding span-averaged wall pressure coefficient distributions are included in figure 11. The development of the LEV structure is very rapid, occurring in the span of $\Delta\alpha = 0.2°$ ($\Delta t = 0.07$, figure 9). Experimental evidence for the LEV structure is mixed, given the difficulty in capturing such a small, rapidly developing flow feature. However, it is alluded to in the classical sketches in Carr *et al.* (1977) through the depiction of a small vortex near the leading edge following the upstream spread of turbulent separation. Furthermore, at a similar Reynolds number on the OA209 airfoil, Mulleners & Raffel (2013) described a 'primary instability stage' whereby, after reverse flow spread over much of the airfoil chord, the shear layer broke down into a system of substructures that mutually engulf each other to form a single DSV structure. Although no specific inference was made to an LSB in their work, a small vortex emanating from the leading edge is observed which convects downstream at a rate much quicker than the other similarly sized vortices. Previous research on this airfoil (Richez *et al.* 2008; Le Pape *et al.* 2012), spanning the same flow conditions, specifically focused on the presence and behaviour of a small leading-edge LSB, indicating a similar boundary-layer topology as that described in the current

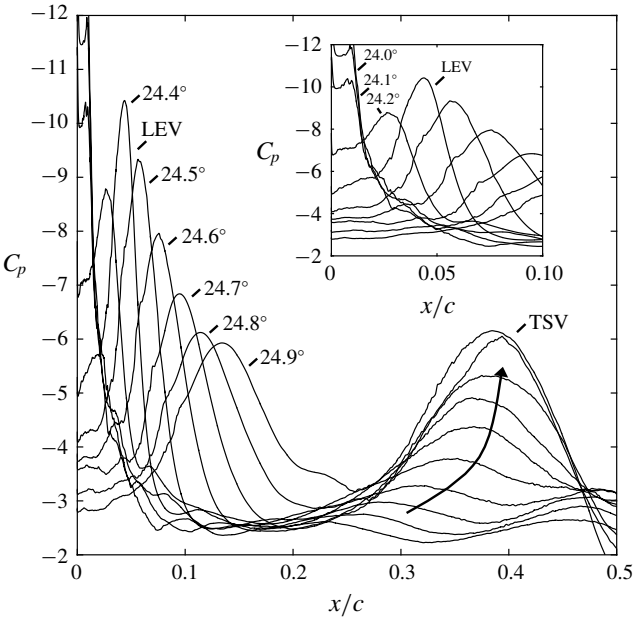

FIGURE 11. Suction-surface pressure coefficient showing suction collapse, LEV development and TSV development. Time instances approximately correspond to the contours in figure 10.

computations. It should be noted that of the various pitching motions analysed in Mulleners & Raffel (2013), the maximum pitch rate is a factor of 2–3 less than that used in the current study. At the same pitch rate and ramp-type motion as that of the current study, Gupta & Ansell (2018), using particle image velocimetry, show both leading-edge and turbulent-separation vortices which interact to form the DSV.

A distinct suction peak associated with the LEV is apparent starting at $\alpha = 24.2°$ at $x/c = 0.03$ in figure 11. Up to $\alpha = 24.4°$ the magnitude of the suction peak grows in strength and then begins to weaken and widen as the LEV convects downstream and departs from the airfoil surface. For a small region of the flow just downstream of the LSB ($0.025 \leqslant x/c \leqslant 0.10$) a distinct 'spike' or 'suction transient' is observed in the wall pressure coefficient as a function of α (see figure 12, marked 'LEV'). Skin-friction coefficient time histories in figure 12 show that this event is associated with strong reverse flow corresponding to the passing of the LEV. The histories at $x/c = 0.03$ are initially downstream of the LSB at the point at which the bursting occurs. Tracking the extrema of these events shows that the LEV initially convects downstream at a velocity of $0.48U_\infty$. Recent experimental data have captured this pressure transient in a high-frequency wall pressure signal (Gupta & Ansell 2018) and it is also noted in the work of Leishman (1990) who provided wall pressure data for a single cycle of the pitching motion. This sharp transient associated with the LEV is most easily visualised just downstream of the LSB reattachment as the LEV develops, where the slow roll off in suction is distinct from the rapid suction as the LEV passes (figure 12, $x/c = 0.03$–0.05). The brief pressure minimum is also visible in figure 6(*b*) in the plots of $C_{p,min}$ where the LEV development temporarily increases the peak suction level after the collapse of leading-edge suction. Also visible in figure 12 at $x/c = 0.01$ is a period of rapid pressure fluctuation prior to suction

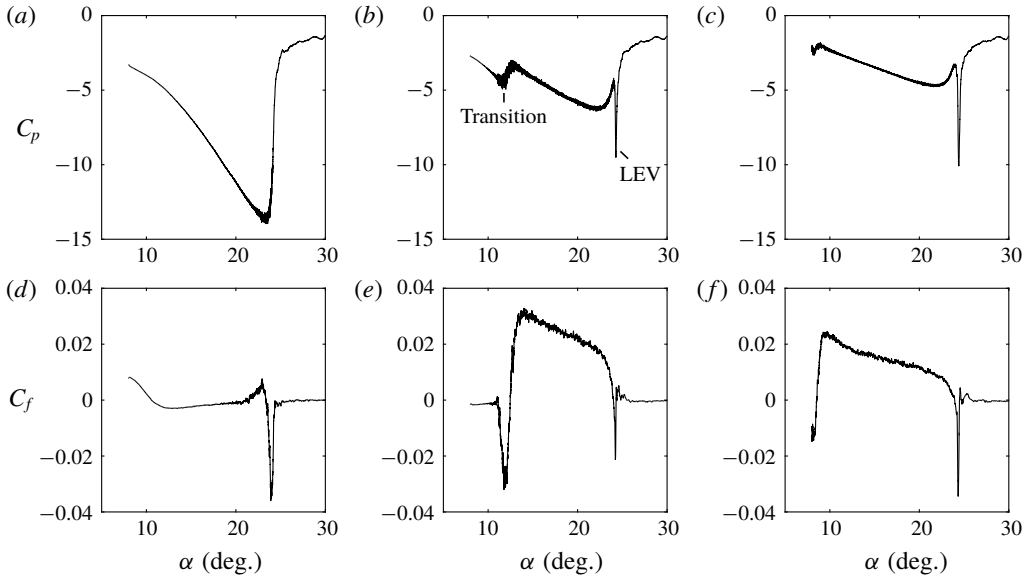

FIGURE 12. Span-averaged wall pressure coefficient (upper) and skin-friction coefficient (lower) at $x/c = 0.01$, 0.03 and 0.05 (left to right) as a function of α. A moving mean filter with a time window of 0.02 is applied to the skin-friction coefficient to better visualise sharp transitions.

collapse. This is noted in the experiments of Lorber & Carta (1988) at $Re_c = 2.0 \times 10^6$ and has been shown to be associated with increased acoustic radiation emanating from the LSB which may be considered as a precursor to the onset of dynamic stall (Visbal & Garmann 2018).

A second feature in figure 10 is the TSV structure that develops over approximately $\Delta\alpha = 0.5°$ ($\Delta t = 0.17$). This structure develops due to the roll up of the turbulent separated boundary layer. Starting at $\alpha = 24.5°$, when the suction peak is beginning to decay (figure 6*b*), the turbulent shear layer appears to break up into a system of separate structures. At least four structures are noted clearly in the contours of entropy. These structures then wrap up together to form the TSV structure ($\alpha = 24.8°$, figure 10). This agrees well with the so-called 'primary instability' mechanism captured by Mulleners & Raffel (2013). Figure 11 shows a distinct suction peak associated with the TSV starting at $\alpha = 24.5°$. At approximately $x/c = 0.35$ this peak only slightly moves downstream as it develops in strength.

Figure 13 shows a comparison of vorticity contours contrasted against entropy contours for select stages within the LEV and TSV development process. This depiction highlights the increased strength and coherence of the LEV as compared to the TSV, something which is somewhat obscured through the entropy visualisations. This imbalance in strength sets the dynamics that occurs during the merging process.

4.6. *Merging of LEV and TSV*

The merging of the LEV and TSV structures is described next. This interaction is key in setting the initial position and strength of the DSV prior to its convection downstream, which is important for the prediction of the force histories throughout the unsteady motion.

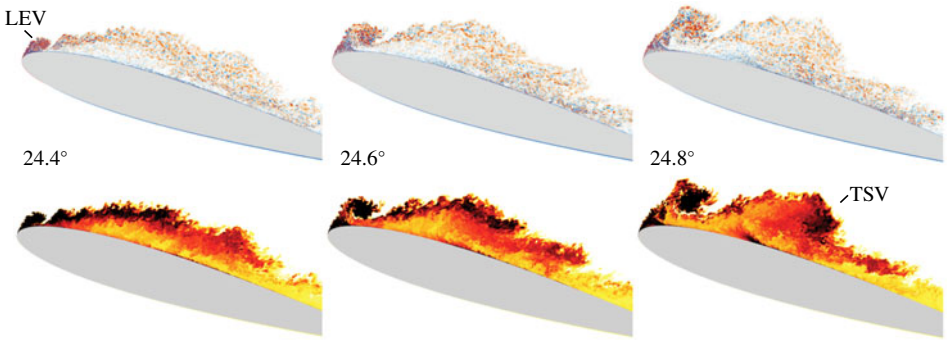

FIGURE 13. (Colour online) Comparison of contours of vorticity (upper) compared to entropy (lower) highlighting strength and coherence of LEV compared to TSV.

The origin of both the TSV and LEV structures is the generation of strong clockwise vorticity in the favourable pressure gradient region of the boundary layer between the stagnation point and the location of peak suction. Until the development of the LEV from the LSB breakdown, the separated turbulent shear layer is continuously fed by the leading-edge vorticity source. This continues as the TSV begins to develop, however at the point at which LEV development occurs, this source of vorticity no longer feeds the TSV resulting in a saturation of total circulation of this structure. Instead leading-edge vorticity feeds the LEV structure which grows in strength to a point at which its total circulation is of similar order to the TSV before it detaches to move downstream.

As the LEV begins to move downstream, the TSV structure is pulled upstream and swept underneath the LEV structure, causing the LEV to lift further from the airfoil surface. This is illustrated from $\alpha = 24.9°$ to $\alpha = 25.5°$ in figure 14. Over this same time period figures 15 and 16 show the merging of the local suction peaks associated with these turbulent structures. At $\alpha = 24.9°$, the suction peak associated with the LEV is positioned at $x/c = 0.12$ and the TSV at $x/c = 0.4$. Through the merging process the TSV suction peak is pulled upstream and the two peaks merge at $x/c = 0.25$. At this point ($\alpha = 25.5°$) the two vortex cores (visualised using entropy, figure 14) have yet to merge, but are simply stacked on top of each other. As the cores merge, the suction peak associated with the DSV decreases in strength, widens slightly and begins to convect downstream. A convection speed of $0.25U_\infty$ was estimated for the DSV based upon x-location of minimum C_p over the time window $6.6 \leqslant t \leqslant 8.0$.

This process, which sets the initial location of the DSV at $x/c = 0.2$–0.3, occurs over the span $24° \leqslant \alpha \leqslant 26°$ in which the average location of the wall suction related to the vortex structures is primarily fixed. The effects of this interaction are observed in the force histories in figure 3, where the roll off of the moment coefficient is briefly reversed and a high normal force coefficient is maintained. As the airfoil continues to pitch above $\alpha = 26°$ the DSV begins to convect downstream, shifting the location of peak suction. Accurate prediction of these events leading to the initial DSV location is important to predict the later time series of the forces in which the strength and position of the DSV is paramount. A similar observation of an extended time period of vortex amalgamation prior to downstream convection is included in Pruski & Bowersox (2013). For the NACA 0012 airfoil at $Re_c = 1.0 \times 10^6$, Pruski & Bowersox (2013) discuss observations of a seemingly 'suspended' DSV that 'forms and gathers strength'.

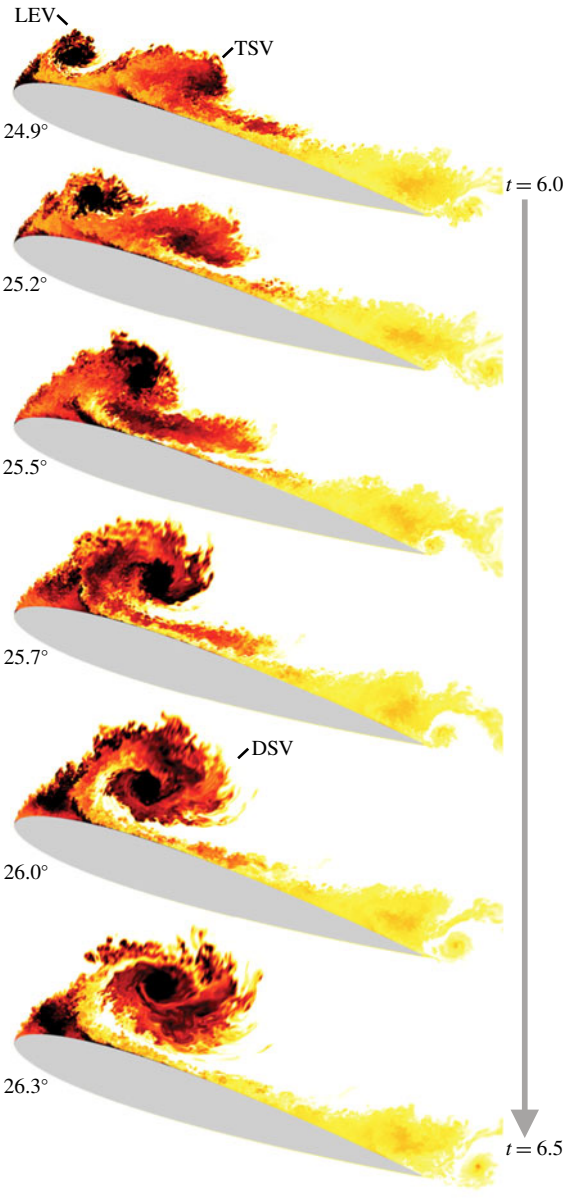

FIGURE 14. (Colour online) Contours of entropy showing merging process of the LEV and the TSV.

The span-averaged wall pressure coefficient versus α is plotted in figure 17 over the range $x/c = 0.3$–0.5. It is important to point out that the separate development of the TSV and the fact that it is pulled upstream creates a situation where single-point time histories of wall pressure are difficult to interpret. At $x/c = 0.4$ pressure decreases in association with the development of the TSV. As described previously, this structure is pulled upstream by the LEV and merges to form the DSV. The pressure rises when the TSV moves upstream and then drops again as the DSV passes. The high temporal and spatial resolution of these computations allow for these two events to be fully characterised.

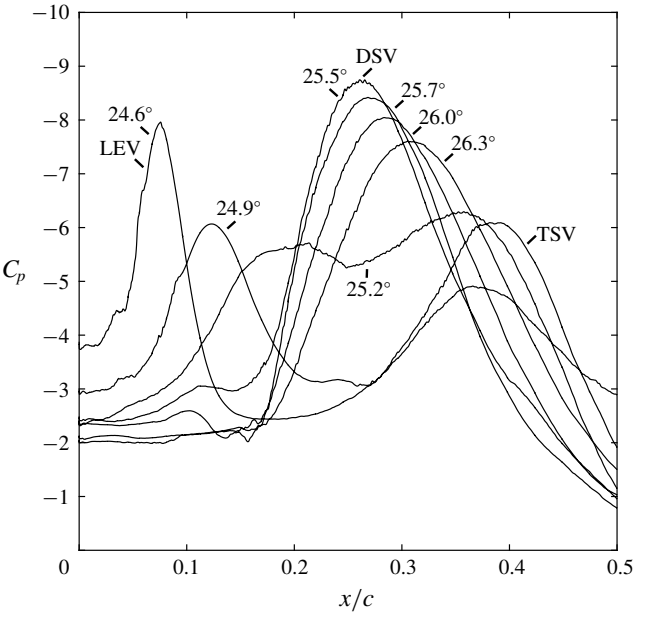

FIGURE 15. Suction-surface pressure coefficient showing merging process between LEV and TSV. Time instances correspond to the contours in figure 14.

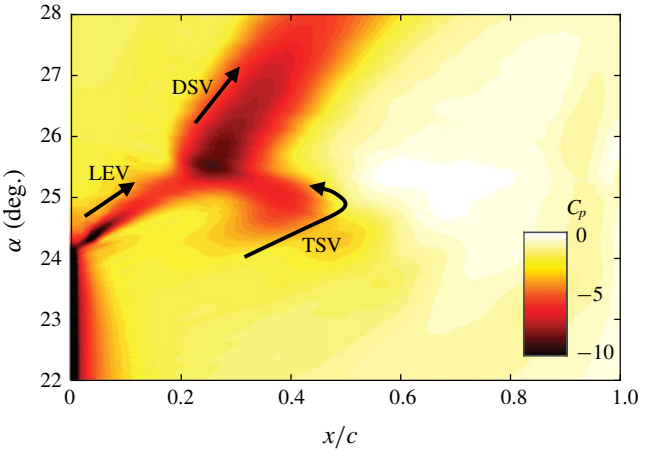

FIGURE 16. (Colour online) Spatio-temporal contour of span-averaged wall pressure coefficient showing the merging process of the LEV and TSV structures.

5. Conclusion

Wall-resolved large-eddy simulations of the unsteady boundary-layer dynamics leading to the onset of dynamic stall on a pitching NACA 0012 airfoil at $Re_c = 1.0 \times 10^6$ have been performed. The boundary-layer development prior to stall is characterised by a contracting LSB and upstream propagation of turbulent separation. Prior to the development of the LEV structure, turbulent separation covers over 95 % of the airfoil surface. At this point, leading-edge suction is still maintained by the

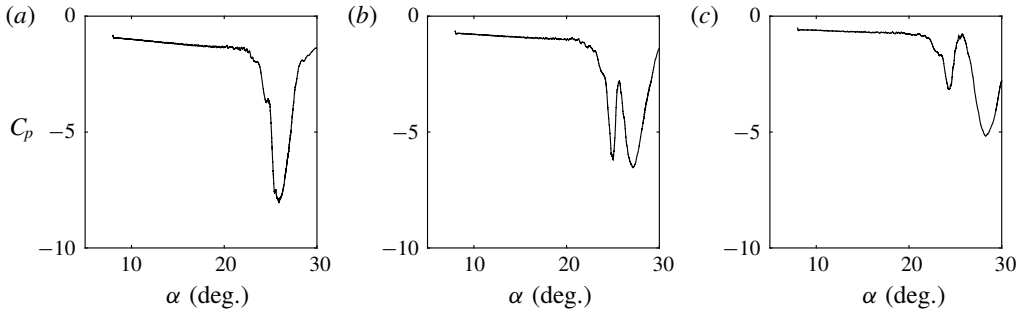

FIGURE 17. Span-averaged wall pressure coefficient as a function of α at $x/c = 0.3$, 0.4 and 0.5 (a–c) showing suction peaks associated with the TSV and DSV structures.

streamline turning provided by the LSB. When the turbulent separation reaches the turbulent reattachment of the separation bubble, airfoil suction suddenly collapses resulting in the rapid generation of the LEV. This structure is small, with diameter of the order of the length of the separation bubble when it initially appears. During this process the turbulent separated shear layer breaks up into a series of vortical structures that coalesce into a single structure (the TSV). This second vortex structure is larger and more diffuse. A complex merging process then takes place where the LEV pulls the TSV upstream. These two structures eventually merge to form the well known DSV.

The generation of a small LEV structure due to turbulent-separation-induced bursting of a small LSB is a feature previously unconfirmed in the literature at these Re_c. This is the cause for the rapid suction transient, visible in the wall pressure signals of Leishman (1984, 1990) and is also likely the mechanism for vortex formation described in Carr *et al.* (1977). At high α it is expected that a small LSB may persist for Re_c as high as 10^7 suggesting that this is a robust stall mechanism. Further examination of the parameter study performed in Leishman (1984) suggests that this behaviour is primarily a form of leading-edge stall unique to dynamic motions.

This stall process at $Re_c = 1.0 \times 10^6$ is contrasted against the stall processes at $Re_c = 0.2$–0.5×10^6 where the DSV develops solely from pressure-gradient-induced bursting of the leading edge LSB. A comparison of all three Re_c shows further upstream penetration of the reverse flow region as Re_c is increased. This characterisation helps to explain the relatively strong sensitivity to Re_c noted within this range in the literature. It also helps to explain the transition from 'classical' leading-edge stall at lower Re_c to the abrupt leading-edge stall process described for $Re_c = 1.0 \times 10^6$.

These complex interactions highlight the need for high-fidelity computations that fully resolve the boundary-layer physics leading to the onset of dynamic stall. Low-order models that predict airfoil forces must take into account these transitional and non-equilibrium events in order to accurately predict the rate and magnitude of force excursions associated with airfoil dynamic stall. Future work to study the sensitivity of this process to motion parameters, airfoil shape, compressibility effects and further increases in Reynolds number is necessary.

Acknowledgements

This work was sponsored in part by AFOSR under Task FA9550-17RQCOR393 monitored by Dr D. Smith and also by a grant of HPC time from the DoD HPC

Block	N_i	N_j	N_k	N_U	Δs_{min}	Δs_{max}	Radial extent	Δn	S/c	Δz
1	2993	294	205	2509	0.00015	0.00050	0.00–0.02	0.000010	0.05	0.00025
2	2096	210	145	—	—	—	0.02–0.25	—	—	0.00036
3	1499	114	105	—	—	—	0.25–1.00	—	—	0.00050
4	901	81	64	—	—	—	1.00–100.0	—	—	0.00085

TABLE 1. Dimensions of the four-block O-grid system for the fine grid.

Shared Resource Centers at AFRL and ERDC. This research was performed while Dr S. Benton held an NRC Research Associateship award at AFRL. Special thanks to Dr D. Garmann of AFRL for assistance in operating FDL3DI.

Supplementary movie

Supplementary movie is available at https://doi.org/10.1017/jfm.2018.939.

Appendix A

This appendix reviews a systematic study of the sensitivity of the results described in the body to various aspects of the computational grid. Three grids of increasing resolution are evaluated both at the static initial condition as well as during the ramp-type pitching motion. Perturbations on the coarse grid including increased resolution in the spanwise direction as well as an extended spanwise domain size to $S/c = 0.1$ (double) and $S/c = 0.2$ (quadruple) are used to demonstrate the sensitivity of the results to these aspects of the grid system. For all results reported in the body of this document, the 'fine' grid with a spanwise extent of $S/c = 0.05$ is used.

A.1. *Grid resolution*

The nested O-grid system of the fine grid is shown in figure 1. The dimensions of this four-block system are given in table 1 along with additional grid spacing values for important aspects of the grid specification. In table 1, N_U refers to the number of points on the airfoil suction surface and Δn refers to the initial wall-normal spacing. Δs refers to the spacing along the airfoil suction surface. Points are clustered (Δs_{min}) near the leading edge to properly resolve the LSB and the transition process. These requirements are slightly relaxed to Δs_{max} as the turbulent boundary layer begins to grow. Grid spacing in the streamwise direction is considerably larger on the pressure surface due to the laminar boundary layer. N_i, N_j and N_k refer to grid dimensions in the azimuthal, wall-normal and spanwise directions respectively, the fine grid is comprised of 267×10^6 nodes.

Using the same grid topology as the fine grid, 'coarse' and 'medium' grids are also developed. These grids total 94 and 174 million points, respectively. Perturbations of the coarse grid are also developed in which the spanwise resolution is increased to that of the fine grid ('Coarse_ZR'), the spanwise domain is doubled ('Coarse_S0.1'), or the spanwise domain is quadrupled ('Coarse_S0.2'). The dimensions and grid spacing values for the inner, body-fitted, block within each these grid systems are given in table 2 to compare against the values used for the fine grid.

For the initial static solution at $\alpha = 8°$, average and maximum values of the wall resolution in wall units are presented in table 3. These values are on the lower end

Grid	Block 1									Total grid size
	N_i	N_j	N_k	N_U	Δs_{min}	Δs_{max}	Δn	S/c	Δz	
Coarse	2264	198	130	1792	0.00020	0.00075	0.000015	0.05	0.00040	93.8×10^6
Coarse_ZR	2264	198	205	1792	0.00020	0.00075	0.000015	0.05	0.00025	147.7×10^6
Coarse_S0.1	2264	198	255	1792	0.00020	0.00075	0.000015	0.10	0.00040	183.1×10^6
Coarse_S0.2	2264	198	505	1792	0.00020	0.00075	0.000015	0.20	0.00040	361.8×10^6
Medium	2589	293	155	2105	0.00015	0.00065	0.000010	0.05	0.00033	173.5×10^6

TABLE 2. Dimensions of the body-fitted interior block of the auxiliary grids used to validate the fine grid in table 1.

Grid	Average			Maximum		
	Δs^+	Δn^+	Δz^+	Δs^+	Δn^+	Δz^+
Coarse	30.0	0.65	17.4	41.6	1.33	35.4
Medium	26.2	0.44	14.7	37.1	0.92	30.6
Fine	19.9	0.45	11.3	30.1	0.95	23.8

TABLE 3. Grid resolution in wall units evaluated at $\alpha = 8°$ within the turbulent portion of the suction surface boundary layer.

Grid	t	α	Δs^+	Δn^+	Δz^+
Coarse	5.25	22.7°	23.7	1.50	39.8
Medium	5.05	22.1°	19.5	1.03	34.5
Fine	4.85	21.6°	20.9	1.10	27.6

TABLE 4. Grid resolution in wall units evaluated at $x/c = 0.025$ at the point in the pitching motion when turbulent separation is near $x/c = 0.25$. Values averaged over a centred time window with width $\Delta t U_\infty/c = 0.1$.

of the range typically put forward in the literature by Piomelli & Balaras (2002) and Georgiadis, Rizzetta & Fureby (2010), indicating sufficient resolution for a wall-resolved LES. Wall units at a higher α are also presented in table 4. Due to the slight mismatch in the onset of dynamic stall for the grids evaluated here, time instances are chosen where turbulent separation has propagated from the trailing edge up to a location of $x/c = 0.25$. The grid resolution in wall units is evaluated downstream of the LSB reattachment point at $x/c = 0.025$. Values are from a span-averaged flow solution and are averaged in time over a centred window with a width of $\Delta t = 0.1$.

The drag coefficient for each grid with a spanwise domain of $S/c = 0.05$ is shown in figure 18(*a*). It is shown that increased grid resolution results in a slightly earlier onset of the dynamic stall process. For each solution the qualitative aspects of the process are unchanged. Through the use of grid Coarse_ZR, it is shown that an increase in z-resolution is a primary driver of this earlier onset. The close agreement between the Fine, Medium, and Coarse_ZR grids suggests convergence of the solutions.

A.2. *Spanwise domain size*

The use of a limited spanwise domain to minimise grid requirements is a common practice in large-eddy simulation of airfoil flows. Visbal & Garmann (2017, 2018)

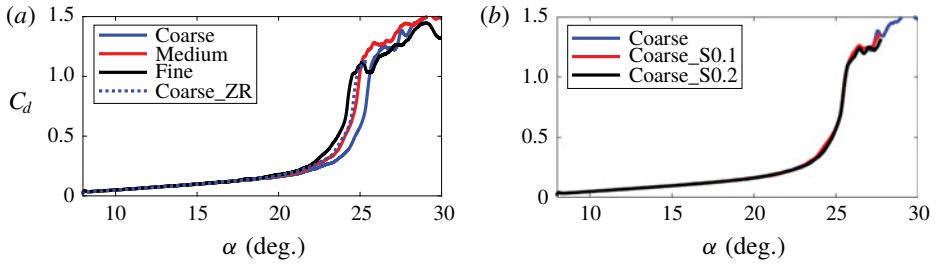

FIGURE 18. (Colour online) Drag coefficient development comparing various grid resolutions (*a*) as well as spanwise domain size (*b*).

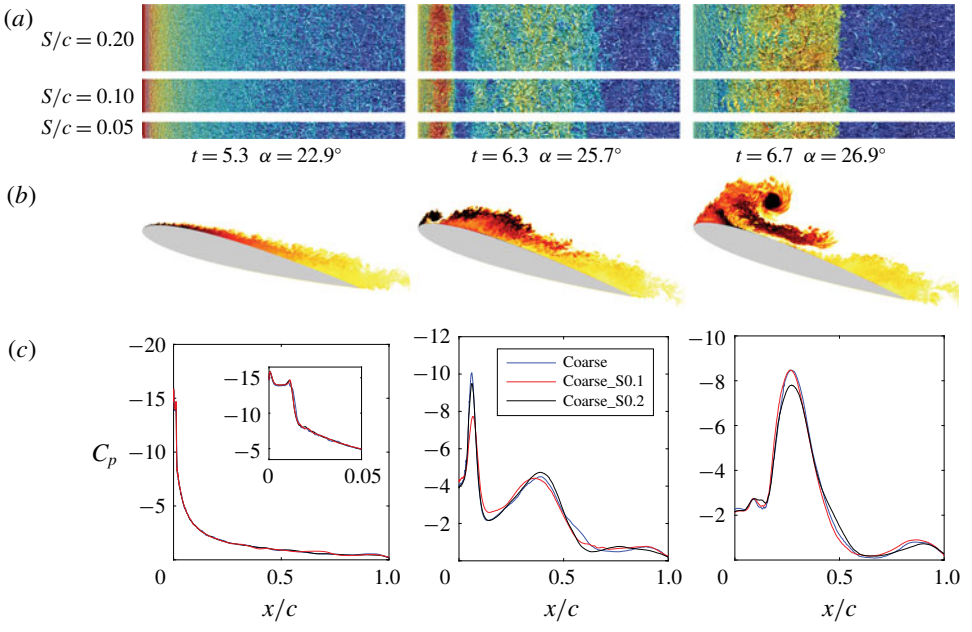

FIGURE 19. (Colour online) Effects of spanwise extent on the 'coarse' grid. Top view of *Q*-criterion iso-surfaces coloured by velocity magnitude (*a*), side views of entropy for reference (*b*) and spanwise averages pressure coefficient on the airfoil suction surface (*c*) at three instances in time covering the development of the DSV.

compared this flow configuration with common wind-tunnel configurations (including a fixed end wall and various end-gap arrangements) and various spanwise domain lengths. It was shown that the spanwise-periodic simulation was able to accurately predict the onset of dynamic stall regardless of end effects or spanwise length (given proper simulation of the turbulent boundary layer prior to stall). The interactions between the dynamic stall vortex and the airfoil trailing-edge flow as well as the reattachment process (for a sinusoidal motion) were highly dependent on spanwise end effects and long-wavelength behaviours not captured in the truncated domain. At a similar high Reynolds number as the current study, Asada & Kawai (2018) evaluated the use of grids with spanwise extent $S/c \leqslant 0.05$. The adverse effects of too small of a span are noted primarily as an accentuated turbulent separation

near the trailing edge, however given proper resolution, little difference was shown between the flow fields for $S/c = 0.0243$ versus $S/c = 0.0493$ indicating $S/c \geqslant 0.025$ is sufficient for these high Reynolds number flows.

A span study is performed here using the coarse grid in the form of a doubled ($S/c = 0.10$) and a quadrupled ($S/c = 0.20$) spanwise domain. The drag coefficient history is shown in figure 18(*b*) and is indistinguishable between the three domain sizes. Figure 19 shows the span-averaged pressure coefficient and top views of Q-criterion for three time instances during the onset of dynamic stall. In each case, very little differences are noted between grids and the flow structure appears fairly spanwise homogeneous. For the purposes of the current study, with a focus on the interactions leading to the onset of dynamic stall, a spanwise extent of $S/c = 0.05$ is deemed appropriate.

REFERENCES

ALPERT, P. 1981 Implicit filtering in conjunction with explicit filtering. *J. Comput. Phys.* **44** (1), 212–219.

ASADA, K. & KAWAI, S. 2018 Large-eddy simulation of airfoil flow near stall condition at Reynolds number 2.1×10^6. *Phys. Fluids* **30**, 085103-22.

BEAM, R. M. & WARMING, R. F. 1978 An implicit factored scheme for the compressible Navier–Stokes equations. *AIAA J.* **16** (4), 393–402.

BENTON, S. I. & VISBAL, M. R. 2017 High-frequency forcing to delay dynamic stall at relevant Reynolds number. In *47th AIAA Fluid Dynamics Conference*. American Institute of Aeronautics and Astronautics.

CARR, L. W. 1988 Progress in analysis and prediction of dynamic stall. *J. Aircraft* **25** (1), 6–17.

CARR, L. W., MCALISTER, K. W. & MCCROSKEY, W. J. 1977 Analysis of the development of dynamic stall based on oscillating airfoil experiments. *Technical Note* NASA TN D-8382. National Aeronautics and Space Administration.

CARR, L. W., MCCROSKEY, W. J., MCALISTER, K. W., PUCCI, S. L. & LAMBERT, O. 1982 An experimental study of dynamic stall on advanced airfoil sections volume 3. Hot-wire and Hot-film measurements. *NASA Technical Memorandum* 84245. National Aeronautics and Space Administration.

CHANDRASEKHARA, M. S., CARR, L. W. & WILDER, M. C. 1994 Interferometric investigations of compressible dynamic stall over a transiently pitching airfoil. *AIAA J.* **32** (3), 586–593.

CHANDRASEKHARA, M. S., WILDER, M. C. & CARR, L. W. 1996 Boundary-layer-tripping studies of compressible dynamic stall flow. *AIAA J.* **34** (1), 96–103.

CRITZOS, C. C., HEYSON, H. H. & BOSWINKLE, R. W. JR 1955 Aerodynamic characteristics of NACA 0012 airfoil section at angles of attack from 0° to 180°. *Technical Note* 3361. National Advisory Committee for Aeronautics.

DIWAN, S. S., CHETAN, S. J. & RAMESH, O. N. 2006 On the bursting criterion for laminar separation bubbles. In *Sixth IUTAM Symposium on Laminar-Turbulent Transition* (ed. R. Govindarajan), pp. 401–407. Springer.

EKATERINARIS, J. A. & PLATZER, M. F. 1997 Computational prediction of airfoil dynamic stall. *Prog. Aerosp. Sci.* **33**, 759–846.

EVANS, W. T. & MORT, K. W. 1959 Analysis of computed flow parameters for a set of sudden stalls in low-speed two-dimensional flow. *Technical Note* NASA TN D-85. National Aeronautics and Space Administration.

GAITONDE, D. V., SHANG, J. S. & YOUNG, J. L. 1999 Practical aspects of higher-order numerical schemes for wave propagation phenomena. *Intl J. Numer. Meth. Engng* **45**, 1849–1869.

GAITONDE, D. V. & VISBAL, M. R. 1998 High-order schemes for Navier–Stokes equations: algorithm and implementation into FDL3DI. *Final Report* AFRL-VA-WP-TR-1998-3060. Air Force Research Laboratory.

GARMANN, D. J., VISBAL, M. R. & ORKWIS, P. 2013 Comparative study of implicit and subgrid-scale model large-eddy simulation techniques for low-Reynolds number airfoil applications. *Intl J. Numer. Meth. Fluids* **71** (12), 1546–1565.

GEORGIADIS, N. J., RIZZETTA, D. P. & FUREBY, C. 2010 Large-eddy simulation: current capabilities, recommended practices, and future research. *AIAA J.* **48** (8), 1772–1784.

GUPTA, R. & ANSELL, P. J. 2018 Investigation of the effects of Reynolds number on the unsteady flow physics of airfoil dynamic stall. In *56th AIAA Aerospace Sciences Meeting*. American Institute of Aeronautics and Astronautics.

HAM, N. D. 1967 Stall flutter of helicopter rotor blades: a special case of the dynamic stall phenomenon. *J. Am. Helicopter Soc.* **12** (4), 19–21.

HAM, N. D. 1972 Some recent mit research on dynamic stall. *J. Aircraft* **9** (5), 378–379.

JONES, B. M. 1934 Stalling. *J. Roy. Aeronaut. Soc.* **38** (285), 753–770.

LE PAPE, A., COSTES, M., JOUBERT, G., DAVID, F. & DELUC, J. M. 2012 Dynamic stall control using deployable leading-edge vortex generators. *AIAA J.* **50** (10), 2135–2145.

LEE, T. & GERONTAKOS, P. 2004 Investigation of flow over an oscillating airfoil. *J. Fluid Mech.* **512**, 313–341.

LEISHMAN, J. G. 1984 Contributions to the experimental investigation and analysis of aerofoil dynamic stall. PhD thesis, University of Glasgow.

LEISHMAN, J. G. 1990 Dynamic stall experiments on the NACA 23012 aerofoil. *Exp. Fluids* **9**, 49–58.

LELE, S. K. 1992 Compact finite difference schemes with spectral-like resolution. *J. Comput. Phys.* **103**, 16–42.

LORBER, P. F. & CARTA, F. O. 1988 Airfoil dynamic stall at constant pitch rate and high Reynolds number. *J. Aircraft* **25** (6), 548–556.

MARTIN, J. M., EMPEY, R. W., MCCROSKEY, W. J. & CARADONNA, F. X. 1974 An experimental analysis of dynamic stall on an oscillating airfoil. *J. Am. Helicopter Soc.* **19** (1), 26–32.

MCALISTER, K. W., CARR, L. W. & MCCROSKEY, W. J. 1978 Dynamic stall experiments on the naca 0012 airfoil. *NASA Technical Paper* 1100. National Aeronautics and Space Administration.

MCALISTER, K. W., PUCCI, S. L., MCCROSKEY, W. J. & CARR, L. W. 1982 An experimental study of dynamic stall on advanced airfoil sections volume 2. Pressure and force data. *NASA Technical Memorandum* 84245. National Aeronautics and Space Administration.

MCCROSKEY, W. J. 1982 Unsteady airfoils. *Annu. Rev. Fluid Mech.* **14**, 285–311.

MCCROSKEY, W. J., CARR, L. W. & MCALISTER, K. W. 1976 Dynamic stall experiments on oscillating airfoils. *AIAA J.* **14** (1), 57–63.

MCCROSKEY, W. J., MCALISTER, K. W., CARR, L. W. & PUCCI, S. L. 1982 An experimental study of dynamic stall on advanced airfoil sections volume 1. Summary of the experiment. *NASA Technical Memorandum* 84245. National Aeronautics and Space Administration.

MCCULLOUGH, G. B. & GAULT, D. E. 1951 Examples of three representative types of airfoil-section stall at low speed. *Technical Note* 2502. National Advisory Committee for Aeronautics.

MULLENERS, K. & RAFFEL, M. 2012 The onset of dynamic stall revisited. *Exp. Fluids* **52**, 779–793.

MULLENERS, K. & RAFFEL, M. 2013 Dynamic stall development. *Exp. Fluids* **54**, 1469-9.

PIOMELLI, U. & BALARAS, E. 2002 Wall-layer models for large-eddy simulations. *Annu. Rev. Fluid Mech.* **34**, 349–374.

PRUSKI, B. J. & BOWERSOX, R. D. W. 2013 Leading-edge flow structure of a dynamically pitching NACA 0012 airfoil. *AIAA J.* **51** (5), 1042–1053.

RICHEZ, F., MARY, I., GLEIZE, V. & BASDEVANT, C. 2008 Near stall simulation of the flow around an airfoil using zonal rans/les coupling method. *Comput. Fluids* **37** (7), 857–866. Special Issue of the 'Turbulence and Interaction-TI2006' Conference.

RIZZETTA, D. P., VISBAL, M. R. & BLAISDELL, G. A. 2003 A time-implicit high-order compact differencing and filtering scheme for large-eddy simulation. *Intl J. Numer. Meth. Fluids* **42** (6), 665–693.

SCHRECK, S. J., FALLER, W. E. & ROBINSON, M. C. 2002 Unsteady separation processes and leading edge vortex precursors: pitch rate and Reynolds number influences. *J. Aircraft* **39** (5), 868–875.

SHELDAHL, R. E. & KLIMAS, P. C. 1981 Aerodynamic characteristics of seven symmetrical airfoil sections through 180-degree angle of attack for use in aerodynamic analysis of vertical axis wind turbines. *Tech. Rep.* SAND80-2114. Sandia National Laboratories.

SHERER, S. E. & VISBAL, M. R. 2007 Multi-resolution implicit large eddy simulations using a high-order overset-grid approach. *Intl J. Numer. Meth. Fluids* **55** (5), 455–482.

STEGER, J. L. 1978 Implicit finite-difference simulations of flow about arbitrary two-dimensional geometries. *AIAA J.* **16** (7), 679–686.

TANI, I. 1964 Low-speed flows involving bubble separations. *Prog. Aerosp. Sci.* **5**, 70–103.

VINOKUR, M. 1974 Conservation equations of gasdynamics in curvilinear coordinate systems. *J. Comput. Phys.* **14** (2), 105–125.

VISBAL, M. R. 2014*a* *Analysis of the Onset of Dynamic Stall Using High-fidelity Large-eddy Simulations*. American Institute of Aeronautics and Astronautics.

VISBAL, M. R. 2014*b* *Numerical Exploration of Flow Control for Delay of Dynamic Stall on a Pitching Airfoil*. American Institute of Aeronautics and Astronautics.

VISBAL, M. R. 2015 *Control of Dynamic Stall on a Pitching Airfoil Using High-frequency Actuation*. American Institute of Aeronautics and Astronautics.

VISBAL, M. R. & GAITONDE, D. V. 1999 High-order-accurate methods for complex unsteady subsonic flows. *AIAA J.* **37** (10), 1231–1239.

VISBAL, M. R. & GAITONDE, D. V. 2002 On the use of higher-order finite-difference schemes on curvilinear and deforming meshes. *J. Comput. Phys.* **181**, 155–185.

VISBAL, M. R. & GARMANN, D. J. 2017 Numerical investigation of spanwise end effects on dynamic stall of a pitching NACA 0012 wing. In *55th AIAA Aerospace Sciences Meeting*. American Institute of Aeronautics and Astronautics.

VISBAL, M. R. & GARMANN, D. J. 2018 Analysis of dynamic stall on a pitching airfoil using high-fidelity large-eddy simulations. *AIAA J.* **56** (1), 46–63.

VISBAL, M. R. & RIZZETTA, D. P. 2002 Large-eddy simulation on curvilinear grids using compact differencing and filtering schemes. *J. Fluids Engng* **124**, 836–847.

VISBAL, M. R. & SHANG, J. S. 1989 Investigation of the flow structure around a rapidly pitching airfoil. *AIAA J.* **27** (8), 1044–1051.

WALLIS, R. A. 1962 Boundary-layer transition at the leading edge of thin wings and its effect on general nose separation. In *Advances in Aeronautical Science*, vol. 3. Pergamon Press.

ZHOU, Y. & WANG, Z. J. 2010 Absorbing boundary conditions for the Euler and Navier–Stokes equations with the spectral difference method. *J. Comput. Phys.* **229** (23), 8733–8749.